Surface analysis of the PrB_6 (001) cleavage plane by scanning tunneling microscopy and spectroscopy

P. Buchsteiner [1], L. Harmsen,[1] M. Ciomaga Hatnean [2], G. Balakrishnan [2], and M. Wenderoth [1,*]

[1]*IV. Physikalisches Institut, Georg-August-Universität Göttingen, 37077 Göttingen, Germany*
[2]*Department of Physics, University of Warwick, Coventry CV4 7AL, United Kingdom*

Scanning tunneling microscopy and spectroscopy were performed on the (001) cleavage plane of praseodymium hexaboride (PrB_6). We found three different ordered morphologies, namely, a chainlike (2×1) reconstruction and two uniform terminations. The chainlike (2×1) reconstruction is rationalized as parallel Pr rows on top of a complete B_6 network. The two uniform terminations are identified as complete Pr or B_6 layers. Although the uniform terminations could be expected to be simply (1×1) reconstructed, one of them shows a rather stripelike atomic corrugation for close tip-sample distances. All morphologies share two spectral features at -0.2 and $+0.2$ eV around E_F. In addition, one uniform termination shows an additional peak in the differential conductance at -0.7 eV. Similarly, the chainlike (2×1) reconstruction reveals a feature in the differential conductance at -1.1 eV when moving the tip closer to the surface. The distance dependency points towards rather localized electronic states, which we tentatively attribute to a $4f$-related feature.

I. INTRODUCTION

For several decades, the surface properties of rare-earth hexaborides (RB_6) have been of steady interest for both technological application and fundamental science. In particular, lanthanum hexaboride (LaB_6) and samarium hexaboride (SmB_6) are in the focus of today's research. LaB_6 has an unusually low work function and is therefore commonly used as an electron emitter [1]. SmB_6 is a Kondo insulator [2,3] with proposed topologically insulating surface states [4]. This variety of physical properties in RB_6 can be traced back to their $4f$ electron occupancy. For instance, La has no occupied $4f$ electron, whereas Sm has a $4f^5$ configuration. In order to further investigate the influence of $4f$ electrons on the surface physics, we add praseodymium hexaboride (PrB_6) as the material of interest in this paper.

From a technological perspective, a thorough understanding of the PrB_6 surface is desired for the growing interest in hexaboride nanocrystals [5–8]. While nanoparticulate LaB_6 is already used as solar control filters [9], nanoparticulate hexaborides are, in general, promising candidates for heat shieldings [8]. Of course, for nanocrystals, the surface-to-bulk ratio is noticeably increased and a thorough understanding of the $4f$ surface physics of hexaborides is inevitable for their practical utilization.

Pr has a $4f^3$ configuration and, as other hexaborides with a partially filled f shell, PrB_6 has an antiferromagnetic ground state [10]. The antiferromagnetic phase transitions occur below $T_N \approx 6.9$ K [11]. However, already at temperatures below ≈ 20 K, short-range ordering occurs [12], which is pinned in the vicinity of boron vacancies [13]. At 10 K, which is well

above T_N, photoemission spectroscopy (PES) has revealed spectral intensity attributed to the occupied $4f$ electrons at around 1 eV binding energy [14,15]. Electronic structure calculations using density functional theory (DFT) of the PrB_6 bulk suggested $4f$ intensity in this energy region as well [16]. Please note that while photoemission experiments typically average over several $(\mu m)^2$ of the investigated surface, the atomic structure of hexaboride surfaces might exhibit various morphologies, as, e.g., observed for LaB_6 [17–19] and SmB_6 [20–27]. Hence, local probe methods such as scanning tunneling microscopy (STM) might be necessary to address the interplay between the $4f$ electrons and the underlying atomic corrugation.

The crystal structure of RB_6 is simple cubic, where the rare-earth ion is situated in the cube's center, as seen in Fig. 1(f). The boron atoms are arranged in octahedra, which are connected by a three-dimensional covalent binding network. The stability of the boron network is established via electron donation of the host metal [28], which inevitably creates an ionic character. Thus, at the resulting surface, a uniform rare-earth or B_6 termination would be polar. The buildup of a polar surface can be avoided by a simple (2×1) reconstruction. This has been reported for LaB_6 [19,29] and SmB_6 [20,24–27], where the rare-earth ions are arranged in parallel chains.

II. METHODS

The experiments were carried out in a home-built scanning tunneling microscope at a base pressure of 6×10^{-11} mbar. Constant current topographies (CCTs) as well as local spectroscopy were acquired at a temperature of 8 K. The PrB_6 single crystal was grown by the floating zone technique, which is described in more detail in [30,31]. The orientation of the single crystal was done by gamma ray diffraction. The crystal

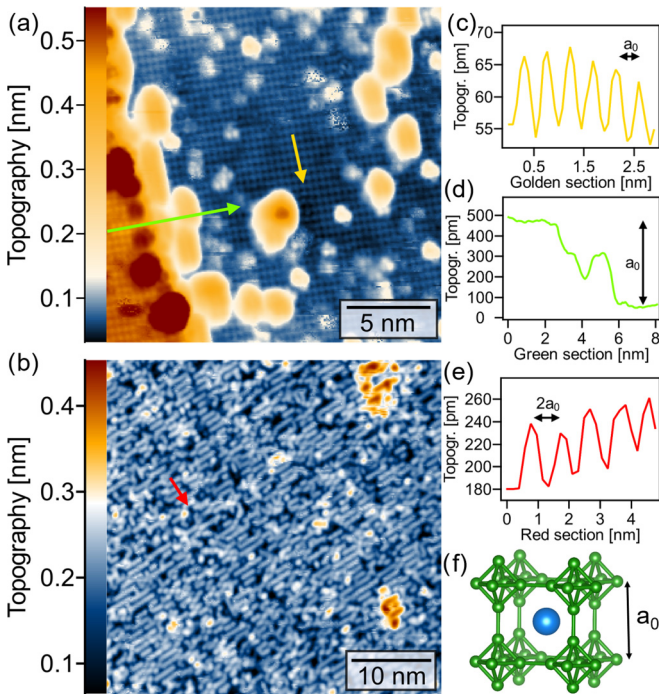*Corresponding author: martin.wenderoth@uni-goettingen.de

FIG. 1. (a) CCT of a surface step taken at 0.4 V/0.1 nA. (b) CCT of a chainlike (2 × 1) reconstructed surface taken at 0.4 V/0.1 nA. (c) Cross section taken along the golden arrow as indicated in (a). (d) Cross section as indicated by the green arrow in (a). (e) Cross section taken along the red arrow as indicated in (b). (f) Crystal structure of PrB_6. The bulk lattice constant of PrB_6 is about $a_0 = 4.1$ Å [11]. The image in (f) was created with VESTA [35].

was cut into sample dimensions of about 1×4 (mm)^2 and 300 μm thickness. The samples were cleaved *in situ* to expose the (001) surface and were transferred immediately into the STM head at 8 K. Tunneling tips were made from electrochemically etched tungsten wire. The tunneling spectra were recorded using a lock-in technique, if not stated otherwise, and the modulation voltages are denoted by V_{mod}. Similar to recent STM studies on other hexaborides, we find the surface to be rather vulnerable. We attribute the high noise level in the presented data explicitly to the sample system. Spatially resolved spectroscopy was rarely successful. Although CCT maps a contour of the integrated local density of states (LDOS) from the Fermi energy up to the applied bias voltage, multibias CCT can provide an estimation for the variation in the LDOS, especially when the $I(V)$ curves show a steep increase for higher bias voltages. The multibias data sets consist of several CCTs, which were acquired quasisimultaneously. The multibias images were not recorded subsequently, but each scan line was recorded with the respective bias voltages before moving to the next scan line. This approach assures that we can exclude tip modification for the interpretation. Additionally, the signal-to-noise ratio of a CCT image can be improved by a so-called template average, as described in [32]. If the CCT image contains a periodic lattice, the periodicity can be used to calculate an averaged unit cell from a given number of examined unit cells. The resulting template topography represents the averaged unit cell, which is periodically extended.

III. RESULTS

Figure 1 shows two large-scale topographies of the PrB_6 (001) cleavage plane. In Fig. 1(a), a uniform terminated surface is presented, which contains a step edge. The respective cross sections are examined in Figs. 1(c) and 1(d). The adjacent surfaces of the step edge are partly covered with disordered protrusions and atomically flat areas extend only over a few (nm)^2. Similar disordered morphologies have been observed on cleaved LaB_6 [19] and SmB_6 [20]. Here, the disordered morphology is examined in the Appendix; see Fig. 5. In Fig. 1(b), the chainlike (2 × 1) reconstruction is shown and a cross section examining the spacing between the chains is shown in Fig. 1(e).

The step in Fig. 1(a) is of one bulk lattice constant a_0 height, which implies that both adjacent terminations are equal. However, determining the surface terminations of PrB_6 is not straightforward. Figure 2 displays three different ordered surface morphologies found on the cleavage surface, namely, a chainlike (2 × 1) reconstruction as well as two uniform terminated structures. We applied multibias CCT as well as local spectroscopy to analyze the electronic properties, which are used to assign the surface terminations.

Figure 2(a) shows a schematic sideview of the chainlike (2 × 1) reconstruction, which is called termination 1 in the following. Ordered atomic rows as observed by CCT [see Fig. 2(b)] are only of a few nm in length and can have a predominant alignment over several-hundred nm. Uniform terminations, as shown in Figs. 2(f) and 2(j), are only observable on areas of a few (nm)^2 with a high density of defects. Scanning tunneling spectroscopy (STS) was utilized to resolve the LDOS for all ordered terminations. Local $I(V)$ curves were acquired and the differential conductance $dI/dV(V)$ is used as an approximation for the LDOS for comparison with PES and DFT results. Figure 2(c) shows the differential conductance around the Fermi energy of the chainlike (2 × 1) reconstruction, which exhibits a finite conductance at the Fermi level and two distinct features at 0.2 and -0.2 eV. In the energy range of ± 1.5 eV, the differential conductance is rather parabola shaped; see Fig. 6 in the Appendix. We expect that the $4f$-related states are rather localized and therefore their wave function does not exceed far into the vacuum. To potentially address these states, we moved the tip closer to the surface by reducing the bias voltage set point. Figure 2(d) shows a spectrum performed with a smaller bias voltage set point of 0.6 V. Here, an additional peak in the electronic structure appears at -1.1 eV.

Termination 2 is shown in Fig. 2(e) and a CCT image is presented in Fig. 2(f). The tunneling spectrum in Fig. 2(g) in the range of ± 0.4 V shows, apart from surface metallicity, two features at about ± 0.2 eV. Additionally, a further spectral feature occurs at -0.7 eV; see Fig. 2(h).

The third termination, as seen in Figs. 2(i) and 2(j), shows only two spectral features at ± 0.2 V; see Fig. 2(k). Opposite to the previous data set of termination 2, no peak at -0.7 eV is observed, which is shown in Fig. 2(l).

The atomic corrugation of the chainlike (2 × 1) reconstruction does not noticeably depend on the applied bias voltage; see Fig. 7 in the Appendix. Similarly, for termi-
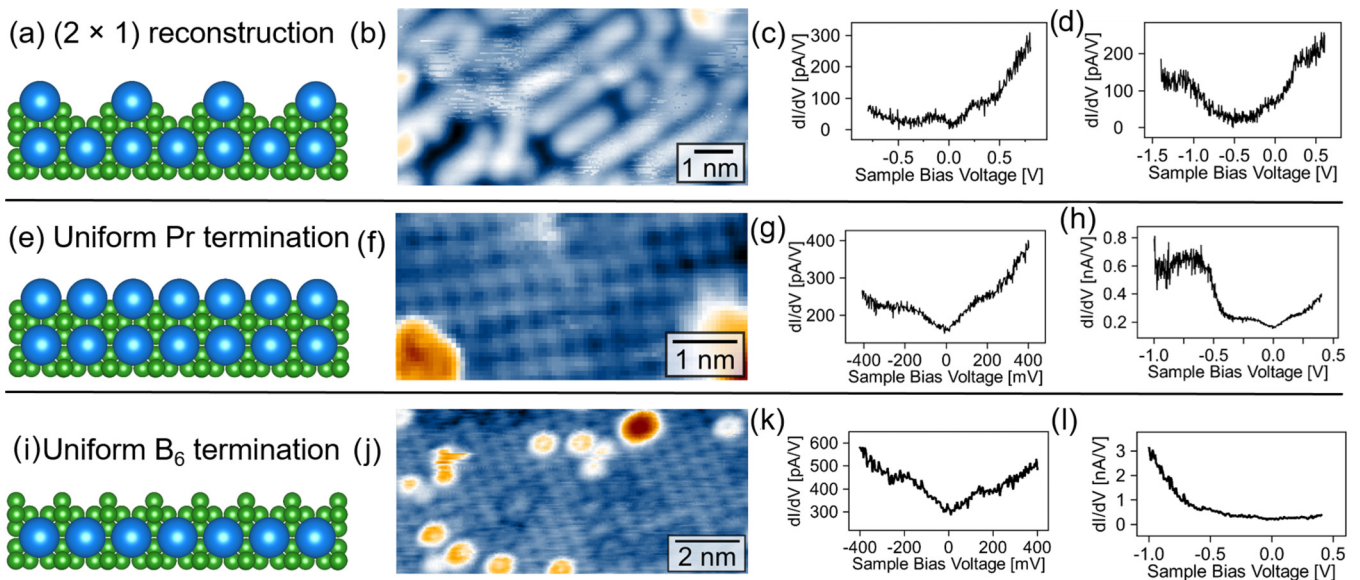
FIG. 2. Overview of the encountered ordered surface morphologies. (a) Schematic sideview of the chainlike (2×1) reconstruction. (b) CCT of the chainlike (2×1) reconstruction taken at 0.4 V/0.1 nA. (c) Tunneling spectroscopy taken on top of an atomic chain, 0.8 V/0.1 nA, and $V_{mod} = 5$ mV. (d) Tunneling spectroscopy taken on top of an atomic chain, 0.6 V/0.1 nA, and $V_{mod} = 5$ mV. (e) Scheme of termination 2, which is assigned as uniform Pr termination. (f) CCT of the uniform Pr termination taken at 1 V/0.1 nA. (g) dI/dV curve taken on top of an atomic protrusion, 0.4 V/0.1 nA, and $V_{mod} = 10$ mV. (h) dI/dV curve taken on top of an atomic protrusion, 0.4 V/0.1 nA, and $V_{mod} = 10$ mV. (i) Scheme of termination 3, which is assigned as uniform B$_6$ termination. (j) CCT of the uniform B$_6$ termination taken at -0.1 V/0.1 nA. (k) The $dI/dV(V)$ curve was taken on top of an atomic protrusion at 0.4 V/0.1 nA, and $V_{mod} = 10$ mV. Furthermore, this spectrum was averaged over 5 spectra. (l) dI/dV curve taken on top of an atomic protrusion, 0.4 V/0.1 nA, and $V_{mod} = 10$ mV. The images in (a), (e), and (i) were created with VESTA [35].

nation 3, the symmetry remains constant upon changing the bias voltage, which is shown in the Appendix as well; see Fig. 9.

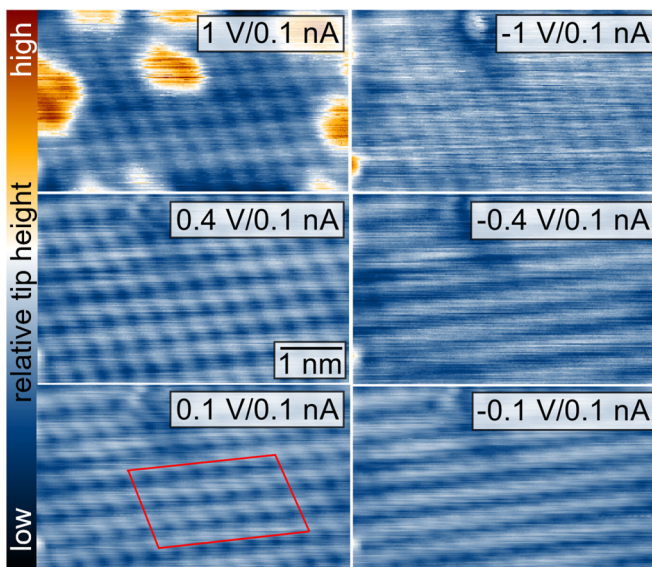In contrast, termination 2 shows a more complex corrugation dependency on the applied bias voltage. Figure 3 displays

FIG. 3. Multibias image of the stripelike reconstructed Pr termination taken at 0.1 nA and ± 1, ± 0.4, and ± 0.1 V. A template topography was made for each CCT image; see Fig. 11 and the respective discussion.

a multibias data set obtained at 0.1 nA and ± 1, ± 0.4, and ± 0.1 V. The atomic corrugation exhibits a (1×1) structure at a set point of 1 V and 0.1 nA. Reducing the bias voltage to 0.4 V leads to a rather ellipselike atomic corrugation, which is further elongated at 0.1 V. This effect is even more pronounced for negative bias voltages. At -0.1 and -0.4 V, the atomic corrugation appears as stripes and with barely any modulation in the fast-scan axis. At -1 V, the high noise level dominates the CCT image. In conclusion, a stripelike corrugation is observed closer to the Fermi level and for the occupied states. A template average of this multibias data set can be seen in the Appendix; see Fig. 11.

Please note that for the 1 V CCT, the atomic corrugation is partly covered with clusterlike protrusions. These defects become seemingly transparent at lower bias voltages, which is discussed in the Appendix in Fig. 5.

By reducing the bias voltage, the tip is brought closer to the surface. Another control of the tip-surface distance can be done by varying the tunneling current. By increasing the tunneling current by 50% to 0.15 nA, a stripy appearance can already be observed at 1 V; see Fig. 4 and Fig. 10 in the Appendix. At 0.4 V/0.15 nA, the atomic corrugation is even more stripelike shaped. At -0.4 V/0.15 nA, neither the (1×1) nor the stripes, but a rather complex corrugation, is observed. The corrugation becomes stripelike again at the set point of -1 V/0.15 nA. Fig. 11 in the Appendix shows a template average of this multibias data set as well. Please note additionally that the multibias images in Figs. 3 and 4 were taken on two different samples with two different tunneling tips.
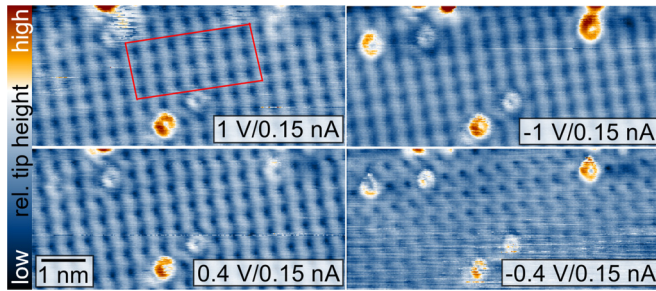
FIG. 4. Multibias image of the stripelike reconstructed Pr termination taken at 0.15 nA and ± 1, ± 0.4 V. A template topography was made for each CCT image; see Fig. 11 and the respective discussion.

IV. DISCUSSION

In summary, the STM experiments revealed the presence of three different ordered surface terminations. A chainlike (2×1) reconstruction has been observed for LaB_6 [19] and SmB_6 [20,24–27] as well, and has been assigned as parallel rows of rare-earth ions on top of a B_6 lattice. The long-range stability of this reconstruction is explained by avoiding the buildup of an electrical potential since it is made from alternating positively charged Pr and negatively charged B_6 units. Consequently, we assign the observed chainlike (2×1) reconstruction as half-terminated Pr rows.

The tunneling spectra of this surface show two features near E_F, namely, at 0.2 and -0.2 eV. Our previous study on the LaB_6 (001) cleavage plane revealed a surface resonance of the chainlike (2×1) reconstruction below E_F stemming from the boron dangling bonds [19]. Here, we propose that the observed feature at -0.2 eV has the same origin. This idea needs to be confirmed by, e.g., DFT calculations. By moving the tip closer to the surface, an additional feature at -1.1 eV arises, which we tentatively describe as a $4f$-related feature. This finding is consistent with photoemission experiments [14,15] and bulk calculations [16] proposing the presence of $4f$ states in this energy range. But by comparing photoemission results with the STS presented here, one has to take into account that PES typically averages over several $(\mu m)^2$. On the other hand, ordered surface terminations have been found only on a spatial scale of a few $(nm)^2$ and the majority of the encountered surface areas appear rather disordered. Furthermore, bulk calculations are not sufficient to describe the surface electronic structure due to the presence of boron dangling bonds, as seen, for instance, for LaB_6 [19] and EuB_6 [33]. Therefore, we cannot unambiguously exclude that the peak at -1.1 eV has a different orbital origin, e.g., it is a boron dangling bond state.

For termination 2, its most prominent spectral feature is the dI/dV (V) peak at -0.7 eV, which is again energetically close to the PES and DFT results for $4f$-related states. Additionally, two spectral features ± 0.2 eV around E_F are present.

Interestingly, the atomic corrugation deviates from a (1×1) structure. This has become apparent when moving the tip closer to the surface, either by bias voltage reduction or an increase of the tunneling current. The atomic corrugation develops to the rather stripelike appearance in one crystallographic direction and stays well modulated in the

perpendicular crystallographic direction. As this stripelike reconstruction emerges for close tip-sample distances, we propose that it also originates from the $4f$ electrons. Combining these findings, it is likely that this surface termination is Pr terminated since the $4f$ electrons are hosted by the Pr ions. As reported, short-range magnetic ordering emerges below ≈ 20 K [12] close to boron defects [13]. Strictly speaking, boron defects are created by the cleavage itself at the surface. Therefore, the occurrence of the stripelike reconstruction at the surface might have a magnetic origin. Interestingly, the formation of local moments at a hexaboride surface has been observed on the EuB_6 (001) cleavage plane [34]. But to this point, the underlying mechanism of the stripelike appearance needs further investigation to clarify whether it is an orbital rearrangement or whether it is induced by magnetic order.

The third termination shows a simple (1×1) symmetry and has two peaks in the differential conductance at ± 0.2 eV. Following the arguments above, this surface has to be B_6 terminated. This is supported by the absence of any peaked spectral weight below E_F at -0.7 eV. Furthermore, if the stripelike appearance would originate from an ordering of the magnetic moments, it is reasonable that it is not seen on a B_6 terminated surface.

Nevertheless, complementary techniques such as angle-resolved photoemission experiments or electronic structure calculations, which include different surface terminations, are required to unambiguously clarify the chemical nature of these observed terminations and their spectral properties.

V. CONCLUSION

RB_6 is a fascinating class of materials exhibiting diverse physical properties and understanding the surface physics is key for their technological utilization. In this paper, we have shown an atomic-scale study of the antiferromagnetic $4f$ electron system PrB_6. By investigating the (001) cleavage plane using STM and STS at low temperature under UHV conditions, we found, in addition to a widely rough and defect-rich surface, three ordered surface morphologies hosting distinctive structural and spectral features.

APPENDIX A: DISORDERED MORPHOLOGY

On the PrB_6 (001) cleavage plane, atomically ordered surface areas have to be searched for and occur rather infrequently. In most cases, the surface appears to be rough and rather disordered. In the following, some of these disordered morphologies are examined.
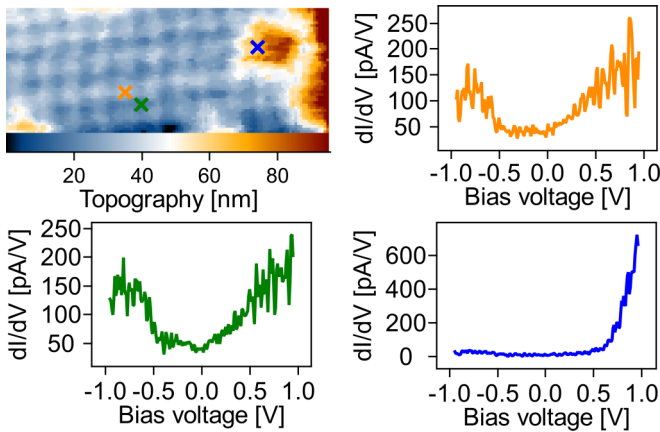
FIG. 5. On the CCT image taken at 1 V/0.1 nA, spatially resolved spectroscopy measurements were performed. The orange spectrum was taken on top of an atomic protrusion, the green spectrum on a hollow site, and the blue spectrum on a disordered protrusion. The spectra shown were obtained without lock-in amplification and are averaged over 3×3 individual dI/dV curves.

FIG. 6. (a) CCT of the chainlike (2×1) reconstruction, taken at 0.4 V and 0.1 nA. (b) Tunneling spectrum taken at 0.8 V, 0.1 nA, and $V_{\mathrm{mod}} = 5$ mV. (c) Tunneling spectrum taken at 0.6 V, 0.1 nA, and $V_{\mathrm{mod}} = 5$ mV. (d) Tunneling spectrum taken at 1.5 V, 0.1 nA, and $V_{\mathrm{mod}} = 5$ mV. All spectra were taken on top of an atomic chain.

Locally resolved tunneling spectroscopy $dI/dV(V, x, y)$ was made on the same Pr terminated area of Fig. 3 and three exemplary spectra are shown in Fig. 5. The orange spectrum was taken on an atomic protrusion and the spectral features at -0.2 and -0.7 eV coincide with the previously shown lock-in spectra in Figs. 2(g) and 2(h). The spectrum at the hollow site, i.e., the green dI/dV curve, is similar to the dI/dV curve taken on top of the atomic corrugation. The spectrum taken at the disordered protrusion, i.e., the blue dI/dV curve, shows a different behavior, namely, high dI/dV values above 0.6 V and almost vanishing dI/dV values below. Therefore, we hypothesize that these protrusions are addressed at bias voltages above 0.6 V, whereas at smaller bias voltages, the atomic lattice is addressed. This is in agreement with the apparent disappearance of the cluster in the multibias data set; see Fig. 3.

The high number of defects and the mostly disordered occurring surface are in agreement with the observations on cleaved LaB$_6$ [19] and SmB$_6$ [20]. The hexaborides are made of a fully three-dimensional covalent binding network and a natural cleavage plane is missing. Therefore, the cleavage can happen in between or within the octahedra and the surface tends to appear rough on the atomic scale. The ordered surface terminations, on the other hand, are often polar. Even for the nonpolar chainlike (2×1) reconstruction, the atomic chains are only of a few nm length and frequently interrupted by defects. Consequently, we find the surface to be rather vulnerable. Furthermore, noise has been a significant problem in our data acquisition on hexaborides. Already in our previous study on LaB$_6$ [19], we stated in the discussion that "we find rather unstable tunneling conditions for negative bias voltages." Additionally, we had difficulties obtaining tunneling spectra for a larger range than ± 1 V. Similar behavior is found for PrB$_6$.

On both uniform terminations, ringlike defects are present (see Figs. 4 and 9). Such defects have been observed on cleaved SmB$_6$ as well and were attributed to disrupted boron
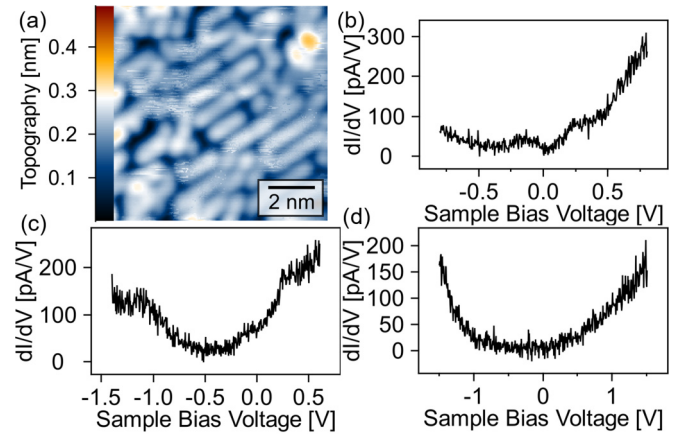
structures [21,22]. Here, on cleaved PrB$_6$, we believe that the same origin seems likely.

APPENDIX B: SUPPORTING DATA OF THE ORDERED SURFACE TERMINATIONS

Figure 6 shows a spectroscopy data set of the chainlike (2×1) reconstruction, and in Fig. 7 a multibias data set of the chainlike (2×1) reconstruction is shown. As stated above, no corrugation change can be observed for the applied bias voltages.

On a cubic surface, no preference between a (2×1) or (1×2) orientation should be present. To investigate the influence of surface defects on the major alignment, Fig. 8 shows two steps between chainlike (2×1) reconstructed areas. In
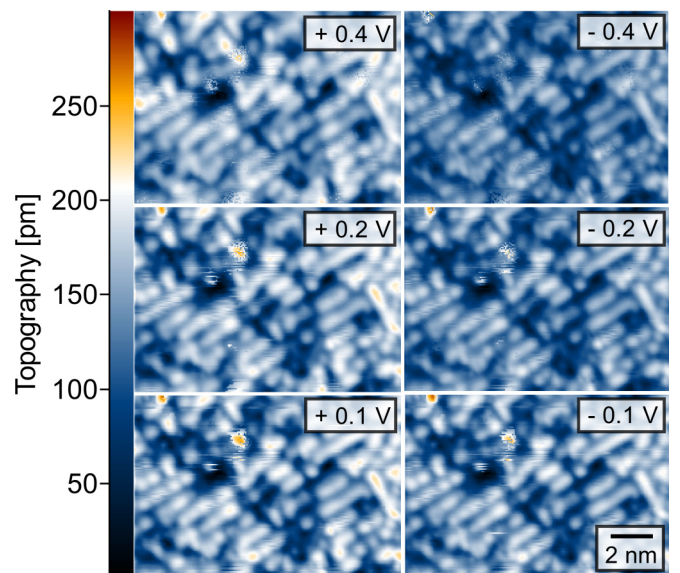

FIG. 7. Multibias data set of the chainlike (2×1) reconstruction. The images were obtained at ± 0.4, ± 0.2, and ± 0.1 V, and at a tunneling current of 0.1 nA.
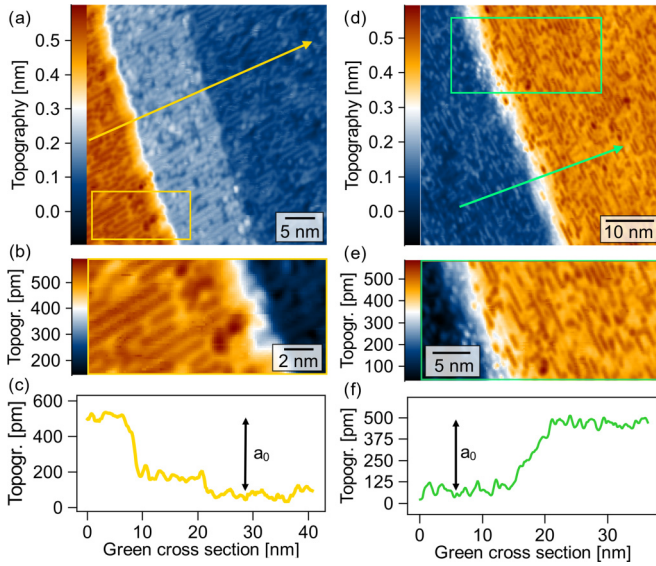
FIG. 8. (a) CCT taken at 0.4 V/0.1 nA. The predominant alignment of the rows is perpendicular to the step edge. (b) Magnification of the golden-colored area in (a). (c) Cross section as indicated by the arrow in (a). (d) The predominant alignment can be arranged parallel to the step edges too, as evident in the high-resolution image seen in (e). CCT in (d) taken at 0.4 V/0.1 nA. (f) Cross section as indicated by the arrow in (d). Please note that in (a), a double-tip artifact is present.

both cases, the step height is one bulk lattice constant [see Figs. 8(c) and 8(f)] and the step edge proceeds vertically [see Figs. 8(a) and 8(d)]. Although the surrounding conditions for the reconstruction seem to be identical, the atomic chains align either (2×1) or (1×2) throughout the step edge. Consequently, we find that the formation of the predominant alignment is independent from the orientation of step edges.

We do not observe a corrugation change of the uniform B_6 termination upon varying the bias voltage. Figure 9 shows a multibias data set of this surface morphology taken at 0.1 nA and ± 0.8, ± 0.4, and ± 0.1 V.
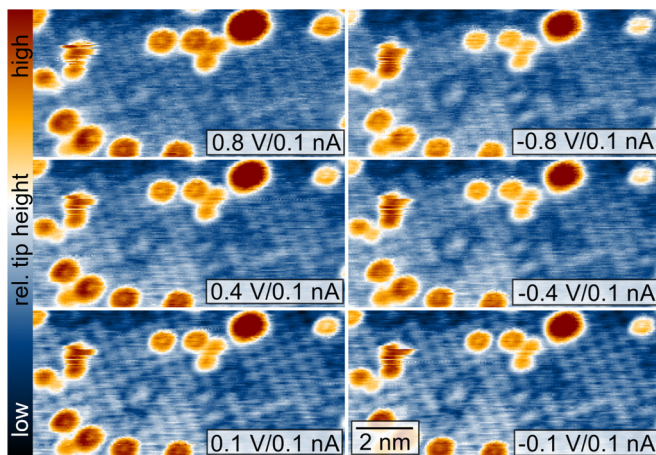

FIG. 9. Multibias CCTs taken at 0.1 nA and ± 0.8, ± 0.4, and ± 0.1 V on the (1×1) reconstructed B_6 surface.
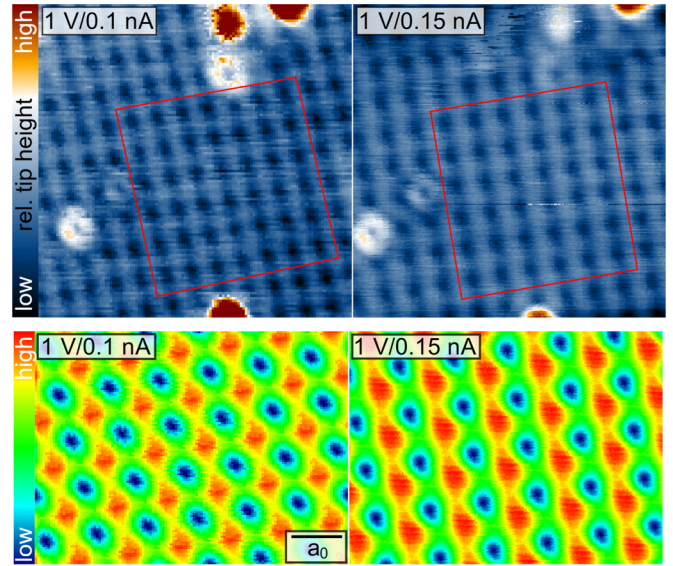

FIG. 10. Top left: CCT image of the Pr terminated surface taken at 1 V/0.1 nA. Top right: CCT image of the Pr terminated surface taken at 1 V/0.15 nA. The reddish enclosed area marks the area where the template average was performed. Bottom left: Template topography made from the CCT on the top left. Bottom right: Template topography made from the CCT on the top right.

In Fig. 10, two CCTs of the uniform Pr termination are shown, which were taken on the same area as Fig. 4. For both images, the bias voltage was set to 1 V, but the tunneling
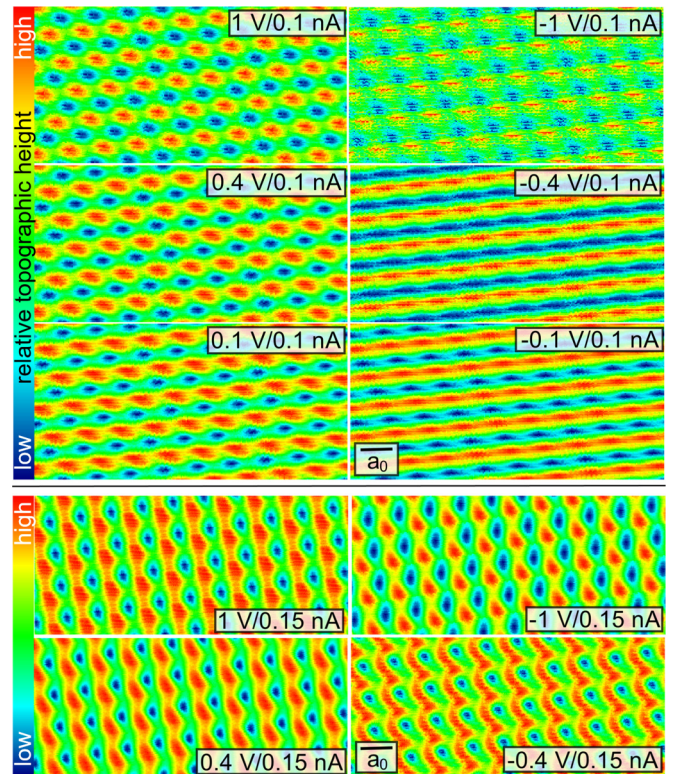

FIG. 11. Template topographies of Fig. 3 at the top and of Fig. 4 at the bottom. The set points are indicated in the respective images.

current for the left image is 0.1 nA and for the right image is 0.15 nA. For both CCT images, a template average was made as well. The apparent corrugation becomes more stripelike by increasing the tunneling current, as evident from the template topographies shown.

Figure 11 shows the template-averaged topographies of Fig. 3 at the top and of Fig. 4 at the bottom, respectively. Here, an averaged unit cell is calculated for each individual CCT from an area, which is enclosed in red in one exemplary CCT image in both Fig. 3 and Fig. 4.

[1] M. Trenary, Sci. Technol. Adv. Mater. **13**, 023002 (2012).

[2] T. Kasuya, Europhys. Lett. **26**, 277 (1994).

[3] S. Souma, H. Kumigashira, T. Ito, T. Takahashi, and S. Kunii, Physica B **312-313**, 329 (2002).

[4] M. Dzero, J. Xia, V. Galitski, and P. Coleman, Annu. Rev. Condens. Matter Phys. **7**, 249 (2016).

[5] H. Takeda, H. Kuno, and K. Adachi, J. Am. Ceram. Soc. **91**, 2897 (2008).

[6] W. Wei, B. Lihong, L. Yingjie, C. Luomeng, and O. Tegus, J. Cryst. Growth **415**, 123 (2015).

[7] M. Zhang, X. Wang, X. Zhang, P. Wang, S. Xiong, L. Shi, and Y. Qian, J. Solid State Chem. **182**, 3098 (2009).

[8] L. Chao, L. Bao, W. Wei, and O. Tegus, Sol. Energy **190**, 10 (2019).

[9] K. Adachi, M. Miratsu, and T. Asahi, J. Mater. Res. **25**, 510 (2010).

[10] T. H. Geballe, B. T. Matthias, K. Andres, J. P. Maita, A. S. Cooper, and E. Corenzwit, Science **160**, 1443 (1968).

[11] C. M. McCarthy, C. W. Tompson, R. J. Graves, H. W. White, Z. Fisk, and H. R. Ott, Solid State Commun. **36**, 861 (1980).

[12] M. Sera, S. Kobayashi, M. Hiroi, N. Kobayashi, and S. Kunii, Phys. Rev. B **54**, R5207(R) (1996).

[13] M. A. Anisimov, A. V. Bogach, V. V. Glushkov, S. V. Demishev, N. A. Samarin, N. Y. Shitsevalova, A. V. Levchenko, V. B. Filipov, A. V. Kuznetsov, and N. E. Sluchanko, Solid State Phenom. **190**, 221 (2012).

[14] S. Patil, G. Adhikary, G. Balakrishnan, and K. Maiti, J. Phys.: Condens. Matter **23**, 495601 (2011).

[15] S. Patil, G. Adhikary, G. Balakrishnan, and K. Maiti, Appl. Phys. Lett. **96**, 092106 (2010).

[16] N. Singh, S. M. Saini, T. Nautiyal, and S. Auluck, J. Phys.: Condens. Matter **19**, 346226 (2007).

[17] J. S. Ozcomert and M. Trenary, Surf. Sci. **265**, L227 (1992).

[18] J. S. Ozcomert and M. Trenary, J. Vac. Sci. Technol., A **10**, 2581 (1992).

[19] P. Buchsteiner, F. Sohn, J. G. Horstmann, J. Voigt, M. Ciomaga Hatnean, G. Balakrishnan, C. Ropers, P. E. Blöchl, and M. Wenderoth, Phys. Rev. B **100**, 205407 (2019).

[20] M. M. Yee, Y. He, A. Soumyanarayanan, D.-J. Kim, Z. Fisk, and J. E. Hoffman, arXiv:1308.1085.

[21] Z. Sun, A. Maldonado, W. S. Paz, D. S. Inosov, A. P. Schnyder, J. J. Palacios, N. Y. Shitsevalova, V. B. Filipov, and P. Wahl, Phys. Rev. B **97**, 235107 (2018).

[22] W. Ruan, C. Ye, M. Guo, F. Chen, X. Chen, G.-M. Zhang, and Y. Wang, Phys. Rev. Lett. **112**, 136401 (2014).

[23] L. Jiao, S. Rößler, D. Kasinathan, P. F. S. Rosa, C. Guo, H. Yuan, C.-X. Liu, Z. Fisk, F. Steglich, and S. Wirth, Sci. Adv. **4**, eaau4886 (2018).

[24] S. Rößler, L. Jiao, D. J. Kim, S. Seiro, K. Rasim, F. Steglich, L. H. Tjeng, Z. Fisk, and S. Wirth, Philos. Mag. **96**, 3262 (2016).

[25] S. Wirth, S. Rößler, L. Jiao, M. V. Ale Crivillero, P. F. S. Rosa, and Z. Fisk, Phys. Status Solidi B, 2000022 (2020).

[26] C. E. Matt, H. Pirie, A. Soumyanarayanan, Y. He, M. M. Yee, P. Chen, Y. Liu, D. T. Larson, W. S. Paz, J. J. Palacios, M. H. Hamidian, and J. E. Hoffman, Phys. Rev. B **101**, 085142 (2020).

[27] H. Pirie, Y. Liu, A. Soumyanarayanan, P. Chen, Y. He, M. M. Yee, P. F. S. Rosa, J. D. Thompson, D.-J. Kim, Z. Fisk, X. Wang, J. Paglione, D. K. Morr, M. H. Hamidian, and J. E. Hoffman, Nat. Phys. **16**, 52 (2020).

[28] H. C. Longuet-Higgins and M. De V. Roberts, Proc. R. Soc. London, Ser. A **224**, 336 (1954).

[29] K. M. Schmidt, O. Jaime, J. T. Cahill, D. Edwards, S. T. Misture, O. A. Graeve, and V. R. Vasquez, Acta Mater. **144**, 187 (2018).

[30] G. Balakrishnan, M. R. Lees, and D. McK. Paul, J. Cryst. Growth **256**, 206 (2003).

[31] G. Balakrishnan, M. R. Lees, and D. McK. Paul, J. Magn. Magn. Mater. **272-276**, 601 (2004).

[32] J. K. Garleff, M. Wenderoth, K. Sauthoff, R. G. Ulbrich, and M. Rohlfing, Phys. Rev. B **70**, 245424 (2004).

[33] S. Rößler, L. Jiao, S. Seiro, P. F. S. Rosa, Z. Fisk, U. K. Rößler, and S. Wirth, Phys. Rev. B **101**, 235421 (2020).

[34] M. Pohlit, S. Rößler, Y. Ohno, H. Ohno, S. von Molnár, Z. Fisk, J. Müller, and S. Wirth, Phys. Rev. Lett. **120**, 257201 (2018).

[35] K. Momma and F. Izumi, J. Appl. Crystallogr. **44**, 1272 (2011).